INSTITUTE OF PHYSICS PUBLISHING PHYSICS IN MEDICINE AND BIOLOGY

Phys. Med. Biol. **51** (2006) 221–236 doi:10.1088/0031-9155/51/2/003

A physical model of multiple-image radiography

Gocha Khelashvili[1], Jovan G Brankov[2], Dean Chapman[3], Mark A Anastasio[4], Yongyi Yang[2,4], Zhong Zhong[5] and Miles N Wernick[2,4]

[1] Center for Synchrotron Radiation Research and Instrumentation, Department of Biological, Chemical and Physical Sciences, Illinois Institute of Technology, Chicago, IL 60616, USA
[2] Department of Electrical and Computer Engineering, Illinois Institute of Technology, Chicago, IL 60616, USA
[3] Department of Anatomy and Cell Biology, College of Medicine, University of Saskatchewan, 107 Wiggins Road, Saskatoon, SK, S7N 5E5, Canada
[4] Department of Biomedical Engineering, Illinois Institute of Technology, Chicago, IL 60616, USA
[5] National Synchrotron Light Source, Brookhaven National Laboratory, Upton, NY 11973, USA

E-mail: brankov@iit.edu

Received 9 August 2005, in final form 24 October 2005
Published 21 December 2005
Online at stacks.iop.org/PMB/51/221

Abstract

We recently proposed a phase-sensitive x-ray imaging method called multiple-image radiography (MIR), which is an improvement on the diffraction-enhanced imaging technique. MIR simultaneously produces three images, depicting separately the effects of absorption, refraction and ultra-small-angle scattering of x-rays, and all three MIR images are virtually immune to degradation caused by scattering at higher angles. Although good results have been obtained using MIR, no quantitative model of the imaging process has yet been developed. In this paper, we present a theoretical prediction of the MIR image values in terms of fundamental physical properties of the object being imaged. We use radiative transport theory to model the beam propagation, and we model the object as a stratified medium containing discrete scattering particles. An important finding of our analysis is that the image values in all three MIR images are line integrals of various object parameters, which is an essential property for computed tomography to be achieved with conventional reconstruction methods. Our analysis also shows that MIR truly separates the effects of absorption, refraction and ultra-small-angle scattering for the case considered. We validate our analytical model using real and simulated imaging data.

1. Introduction

Diffraction-enhanced imaging (DEI) (Chapman *et al* 1997) was the first planar, phase-sensitive x-ray technique to produce separate images of absorption and refraction effects. The DEI

method allows the visualization of weakly absorbing features of soft tissue, which otherwise are obscured by the presence of scattered radiation. Despite the spectacular images produced by DEI, the method has significant drawbacks. Most notably, DEI incorrectly neglects ultra-small-angle x-ray scattering (USAXS), an effect in which microstructure of the object causes small refractive perturbations to the beam. Since biological tissue has structure on the scale needed to create USAXS, DEI images almost always contain artefacts that become very noticeable if used for computed tomography (CT) reconstruction (Brankov *et al* 2004). DEI also assumes a simplified model of the intrinsic rocking curve of the imaging system (which is the angular impulse response function of the crystal optics system). This approximation yields additional artefacts, particularly at strong refraction boundaries. As a result, images produced by the DEI method do not truly portray attenuation and refraction, but instead some nonlinear mixture of these effects with USAXS (Brankov *et al* 2004, Wernick *et al* 2003).

We have proposed the multiple-image radiography (MIR) method (Wernick *et al* 2003) as an alternative to DEI. Similar methods have also been independently proposed by others (Pagot *et al* 2003, Rigon *et al* 2003). MIR corrects errors inherent in DEI (in refraction and absorption images), is more robust to noise than DEI and explicitly produces an additional image of a USAXS parameter, which conveys information about microstructure of the object. We have also extended the planar MIR method to a CT implementation, which yields slice or volumetric images of the object (Brankov *et al* 2004), and we have shown that these images significantly lessen the artefacts seen in DEI CT images.

Although we have made significant progress in applying MIR, we have not yet presented a thorough explanation of the physics of this imaging method. In this paper, we use radiative transport theory to derive expressions for the three MIR image parameters in terms of fundamental properties of the object. To make the problem tractable, we model the object as a collection of discrete scatterers embedded in an inhomogenous medium. Such an approach to modelling of tissue properties has precedent in the area of optical scattering, where discrete scatterers were used to form a tissue-equivalent model (Schmitt and Kumar 1998).

An important goal of this paper is to demonstrate that the MIR image parameters represent line integrals of various quantitative descriptors of the object, which is a necessary condition for implementing CT by conventional means. Another key aim of the paper is to show that the MIR methodology indeed isolates the effects of absorption, refraction and USAXS in the three images that it produces.

In the following section, the MIR method is briefly reviewed. In section 3, we introduce the object model and propagation model. In section 4, we solve the propagation model for our problem, and in section 5 we use this solution to predict the values of the imaging parameters measured by the MIR method. In section 6, we validate the theoretical model experimentally and present conclusions in section 7. Some details of the derivations are provided in appendices A and B.

2. Multiple-image radiography

The MIR imaging technique has been described in detail before (e.g. Wernick *et al* (2003)), but we review the salient features here for completeness. In MIR, as in DEI, the object is illuminated by a highly collimated, quasi-monochromatic x-ray beam, which has been prepared by using diffracting crystals as shown in figure 1. After penetrating the object, the beam strikes a third crystal, called the *analyser*, which diffracts principally the portion of the beam travelling in a particular direction. By rotating the analyser, and collecting images along the way, an angular intensity spectrum of the transmitted beam can be obtained at each pixel. The angular intensity spectrum describes the beam intensity as a function of angle; thus, it

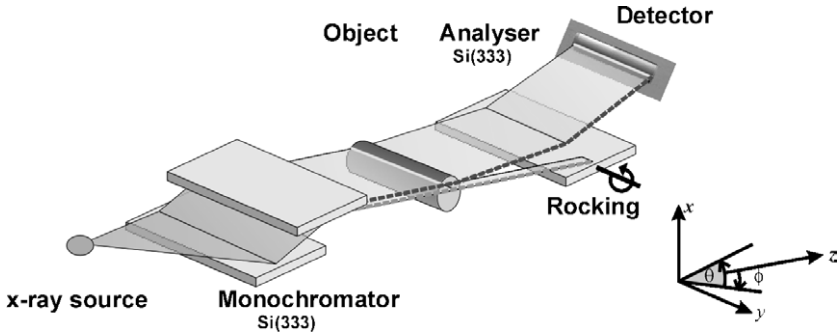

Figure 1. Schematic diagram of the MIR imaging system.

contains the information needed to measure the absorption, refraction and USAXS properties of the object.

In MIR imaging, these properties of the object are assessed at every pixel as follows. The absorption coefficient is inferred from the integral of the beam's angular intensity spectrum (i.e. the total transmitted intensity); the total net refraction angle of the beam is estimated as the displacement of the centroid of the angular intensity spectrum from its direction when the object is absent; and, finally, the angular divergence of the beam caused by USAXS is quantified by the second central moment of the angular intensity spectrum.

By displaying these three parameters, one obtains three distinct images conveying different physical characteristics of the object. Thus, MIR produces a rich description of soft tissue and shows promise for clinical imaging. Owing to the persistence of refraction and USAXS contrast at x-ray energies characteristic of a tungsten source, therefore MIR can be performed at higher energies and, therefore, much lower dose than conventional mammography, which is performed using a molybdenum source. Because MIR eliminates image degradation due to scatter, MIR may also reduce the need for breast compression during mammographic imaging, because it significantly limits scatter, and lessens dose dramatically if used at tungsten energies; however, some breast compression may still be desirable for purposes of limiting superposition of structures.

An example of MIR images is shown in figure 2 to illustrate the MIR technique. The object shown is a human foot, illustrating how MIR clearly shows soft tissues that are not well visualized by conventional radiography.

While MIR imaging appears quite promising, no quantitative theoretical model of the imaging process has yet been developed. The main goal of this paper is to derive expressions for the three MIR parameters (absorption, refraction angle and the USAXS parameter) in terms of the physical object parameters that give rise to them, specifically: the linear absorption coefficients of the medium and scatterers, the index of refraction distribution of the medium and several properties of the scatterers.

Most importantly, we show that all three MIR parameters are line integrals of various descriptors of the object, which is a desirable property that enables MIR to be used in a CT mode. Linearity is also helpful in planar imaging, where it can facilitate meaningful image interpretation.

3. Theoretical model

MIR measures only beam components travelling within microradians of the forward direction. In this regime, interactions are dominated by refractive effects caused by object features that are large compared with the x-ray wavelength. The interference effects due to free-space

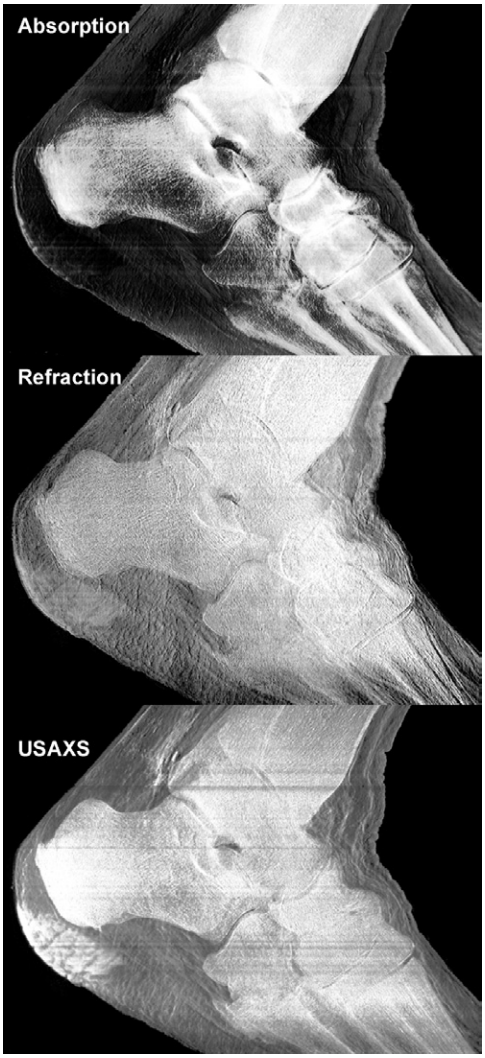

Figure 2. MIR images of a human foot. The MIR absorption image is similar to a conventional radiograph, but exhibits much less scatter degradation. The MIR refraction and USAXS images show soft-tissue structures, such as cartilage, which are poorly visualized, or even invisible, in a conventional radiograph.

wave propagation can be neglected, since the object–analyser and analyser–detector distances are small. Thus, in MIR imaging, the relevant interactions of the x-ray beam with the object are well described by geometrical optics. In such situations, it is convenient to model beam propagation using radiative transport theory (Ishimaru 1997), an approach which accounts for average net energy flows within a medium. We model the object as a stratified medium with discrete scattering centres, as explained in the next section.

3.1. Stratified medium with discrete scattering centres

We model the object to be imaged as a medium characterized by a linear absorption coefficient $\mu(\vec{r}) = \mu(z)$ that is slowly varying in the z-direction and by a spatially varying refractive

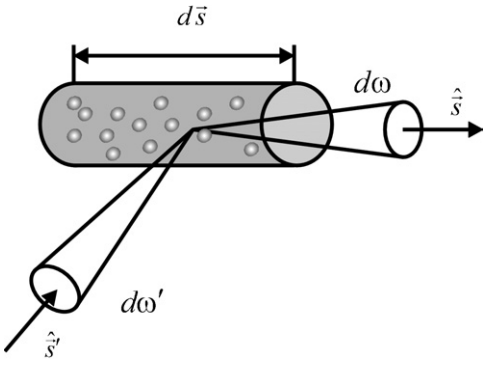

Figure 3. Incoming and outgoing scattering directions and corresponding incremental solid angles.

index $n(\vec{r})$ given locally as a function of x and z by the following:

$$n(\vec{r}) = n_0 + n_x(z)x, \tag{1}$$

where $\vec{r} = (x, y, z)^T$ denotes the spatial coordinates. In equation (1), which is a Taylor-series approximation of a potentially more-complicated refractive-index distribution, the factor $n_x(z)$ is the refractive-index gradient and n_0 is a constant. Note that the medium can have refractive-index variations in the y-direction as well by introducing an appropriate rotation of the coordinate system about the z-axis (see appendix A).

For simplicity, we assume that the object is permeated by a collection of identical discrete scatterers having number density $\rho_n(\vec{r}) = \rho_n(z)$ that is slowly varying in the z-direction. The results that follow can be generalized readily to accommodate the more general case in which the scatterers are not identical. As demonstrated in section 6.1, this is achieved by averaging over the known probability distributions of the particles' properties. Each particle will be characterized by its extinction cross section $\sigma_{ext}(z)\rho_n(z)$ (which is a sum of the scattering cross section $\sigma_s(z)$ and absorption cross section σ_a), and phase function, $p(\vec{r}, \hat{\hat{s}}, \hat{\hat{s}}')$, which is the incremental fraction of radiation scattered from solid angle $d\omega$ in the incoming direction $\hat{\hat{s}}'$ into solid angle $d\omega'$ in the outgoing direction $\hat{\hat{s}}$ (see figure 3). We assume isotropic scattering, which results in a phase function of the form $p(\vec{r}, \hat{\hat{s}}, \hat{\hat{s}}') = p(z, \hat{\hat{s}} - \hat{\hat{s}}')$. The scattering cross section can be described in terms of an effective radius R as $\sigma_s(z) = R(z)^2\pi$. In our calculations, we will use a quantity called *albedo*, which is defined as

$$W_0(z) \triangleq \frac{1}{4\pi}\int_{4\pi} p(z, \hat{\hat{s}} - \hat{\hat{s}}')\, d\omega'(\hat{\hat{s}}') = \frac{\sigma_s(z)}{\sigma_{ext}(z)}. \tag{2}$$

3.2. Radiation transport model

To begin our derivation, let us first define the specific intensity $I(\vec{r}, \hat{\hat{s}})$ as the radiation density of the x-ray beam at position $\vec{r} = (x, y, z)$ in the direction $\hat{\hat{s}} = (\sin\theta\cos\phi,\ \sin\theta\sin\phi,\ \cos\theta)$, where $\vec{r}$ and $\hat{\hat{s}}$ are defined as in figure 4. The propagation of x-rays through the object is described by the following radiative transport equation (see figure 4):

$$\begin{aligned}\hat{\hat{s}} \cdot \nabla_{\vec{r}}\, I(\vec{r}, \hat{\hat{s}}) &= -\mu(\vec{r}) I(\vec{r}, \hat{\hat{s}}) - \rho_n(\vec{r})\sigma_a I(\vec{r}, \hat{\hat{s}}) - \rho_n(\vec{r})\sigma_s(\vec{r}) I(\vec{r}, \hat{\hat{s}}) \\ &\quad + \vec{b}(\vec{r}) \cdot \nabla_{\hat{\hat{s}}} I(\vec{r}, \hat{\hat{s}}) + \frac{\rho_n(\vec{r})\sigma_{ext}(\vec{r})}{4\pi}\int_{4\pi} p(z, \hat{\hat{s}} - \hat{\hat{s}}') I(\vec{r}, \hat{\hat{s}}')\, d\omega',\end{aligned} \tag{3}$$

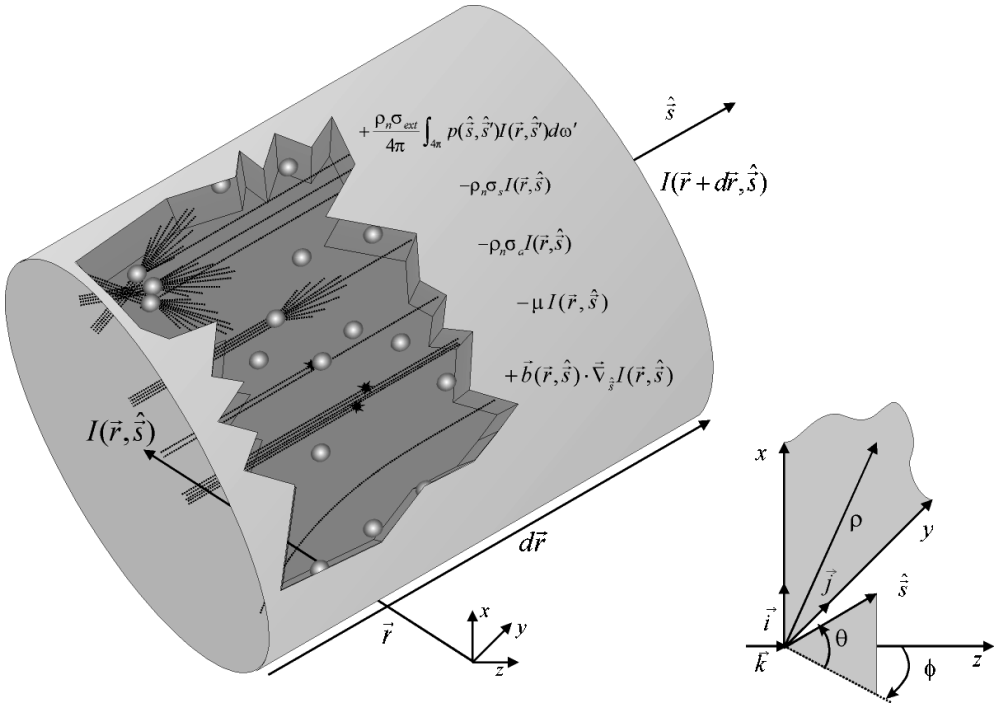

Figure 4. Illustration of terms in the radiation transport equation.

where

$$\vec{b}(\vec{r}) = \nabla_{\vec{r}} \ln n(\vec{r}) \approx \frac{n_x(z)}{n_0 + n_x(z)x}\vec{i} \approx \frac{n_x(z)}{n_0}\vec{i} \triangleq b_x(z)\vec{i} \tag{4}$$

is a constant vector, and $\vec{i}$ is the unit vector in the x-direction.

The first three terms on the right-hand side of equation (3) account, respectively, for radiation loss from the direct beam due to (1) absorption by the medium in which the scatterers are embedded, (2) absorption by the scatterers and (3) scattering from the forward direction into other directions. The fourth term in equation (3) represents the transfer of radiation into the forward direction from other directions by refraction. The last term in equation (3) represents the transfer of radiation into the forward direction from other directions by scattering. An equation similar to equation (3) appears in standard treatments of transport theory such as (Ishimaru 1997); however, these presentations generally omit the fourth term, which describes the refraction effect. The form of this refraction term in equation (3) is not obvious; therefore, we derive it in detail in appendix A.

For radiation propagating in the ultra-small-angle regime (very near the forward direction), a small-angle approximation (Ishimaru 1997) can be made to equation (3), yielding

$$\frac{\partial}{\partial z} I(z,\vec{\rho},\vec{s}) + \vec{s}\cdot\nabla_{\vec{\rho}} I(z,\vec{\rho},\vec{s}) = -(\rho_{\mathrm{n}}(z)\sigma_{\mathrm{a}} + \mu(z))I(z,\vec{\rho},\vec{s})$$

$$+ \vec{b}(z)\cdot\nabla_{\vec{s}} I(z,\vec{\rho},\vec{s}) + \frac{\rho_{\mathrm{n}}(z)\sigma_{\mathrm{ext}}(z)}{4\pi}\iint_{\mathbb{R}^2} \mathrm{d}^2\vec{s}'\, p(z,\vec{s}-\vec{s}')I(z,\vec{\rho}-\vec{s}). \tag{5}$$

4. Solution of the transport equation

The general solution of equation (5), which can be obtained by the Fourier transform method in a manner similar to the derivation is in (Ishimaru 1997), is given by

$$I(z,\vec{\rho},\vec{s}) = \frac{1}{(2\pi)^4}\iint_{\mathbb{R}^2} \mathrm{d}^2\vec{\kappa}\iint_{\mathbb{R}^2} \mathrm{d}^2\vec{q}\,\exp[-(\mathrm{i}\vec{\kappa}\cdot\vec{\rho}+\mathrm{i}\vec{s}\cdot(\vec{q}-\vec{\kappa}z))] \times \exp\left[-\int_0^z (\mathrm{i}\vec{b}(z)(\vec{q}-\vec{\kappa}z)+\mu(z)-\rho_\mathrm{n}(z)\sigma_\mathrm{ext}(z))\,\mathrm{d}z\right] F_0(z,\vec{\kappa},\vec{q})K(z,\vec{\kappa},\vec{q}), \tag{6}$$

where

$$F_0(\vec{\kappa},\vec{q}) = \iint_{\mathbb{R}^2} \mathrm{d}^2\vec{s}\iint_{\mathbb{R}^2} \mathrm{d}^2\vec{\rho}\,I_0(\vec{\rho},\vec{s})\exp(\mathrm{i}\vec{\kappa}\cdot\vec{\rho}+\mathrm{i}\vec{s}\cdot\vec{q}), \tag{7}$$

$$K(z,\vec{\kappa},\vec{q}) = \exp\left[\frac{\rho_\mathrm{n}(z)\sigma_\mathrm{ext}(z)}{4\pi}\int_0^z P(z,\vec{q}-\vec{\kappa}z')\,\mathrm{d}z'\right], \tag{8}$$

and

$$P(z,\vec{q}) = \iint_{\mathbb{R}^2} \mathrm{d}^2\vec{s}\;p(z,\vec{s})\exp(\mathrm{i}\vec{s}\cdot\vec{q}). \tag{9}$$

Assuming a Gaussian phase function for the scatterers we have

$$p(z,\vec{s}) = 4\pi W_0(z)\frac{1}{2\pi|\boldsymbol{\alpha}|^{1/2}}\exp\left(-\frac{1}{2}\vec{s}^T\boldsymbol{\alpha}^{-1}\vec{s}\right) \tag{10}$$

with

$$\boldsymbol{\alpha} = \frac{1}{2}\mathrm{diag}\left(\frac{1}{\alpha_\mathrm{p}},\frac{1}{\alpha_\mathrm{p}}\right), \tag{11}$$

where diag(·) denotes a diagonal matrix containing elements in the bracket and $\alpha_\mathrm{p} = \left[4\delta^2\ln\left(\frac{2}{\delta}+1\right)\right]^{-1}$ is an angular beam broadening due to a single spherical scatterer (von Nardroff 1926). Next it follows that

$$P(z,\vec{q}) = 4\pi W_0(z)\exp\left(-\frac{1}{2}\vec{q}^T\boldsymbol{\alpha}\vec{q}\right). \tag{12}$$

Here it is worth noting that the model assumes that the beam divergence due to a single particle does not depend on the size of the particle because $\boldsymbol{\alpha}$ is not a function of the particle size; however, the phase function does depend on the particle size through $W_0(z)$. This model is valid for scatterers having diameter in the range of 10^4–10^6 times the x-ray wavelength (Ishimaru 1997).

Thus, equation (8) takes the following form:

$$K(z,\vec{\kappa},\vec{q}) = \exp\left(\int_0^z \rho_\mathrm{n}(z)\sigma_\mathrm{ext}(z)W_0(z)\exp\left(-\frac{1}{2}(\vec{q}-\vec{\kappa}z')^T\boldsymbol{\alpha}(\vec{q}-\vec{\kappa}z')\right)\mathrm{d}z'\right). \tag{13}$$

Of course, the assumption of a Gaussian phase function is only an approximation. However, we show in section 6 that the Gaussian assumption provides a good approximation of scattering from spherical particles. The Gaussian assumption can also be motivated on statistical grounds, because the average phase function can be derived as the convolution of the phase functions of individual scatterers, which approximates a Gaussian function by the central limit theorem.

Next, let us assume that the beam incident at the object is a Gaussian beam, i.e.,

$$I_0(z,\vec{\rho},\vec{s}) = I_0\frac{1}{2\pi|\boldsymbol{\beta}|^{1/2}}\exp\left(-\frac{1}{2}\vec{s}^T\boldsymbol{\beta}^{-1}\vec{s}\right), \tag{14}$$

where β describes the initial width of the incident beam and $|\beta|$ is the determinant of the matrix $\beta = \frac{1}{2}\mathrm{diag}\left(\frac{1}{\beta_x}, \frac{1}{\beta_y}\right)$. Substituting from equation (14) into equation (7) we obtain

$$F_0(\vec{\kappa}, \vec{q}) = (2\pi)^2 I_0 \exp\left(-\tfrac{1}{2}\vec{q}^{\,T}\beta\vec{q}\right)\delta(\vec{\kappa}), \tag{15}$$

where $\delta(\vec{\kappa})$ denotes a Dirac delta function. Substituting equations (13) and (15) into equation (6) yields (after integration with respect to $\vec{\kappa}$ and utilizing the properties of the delta function)

$$I(z, \vec{\rho}, \vec{s}) = \frac{I_0}{(2\pi)^2}\exp(-\tau'(z))\iint_{\mathbb{R}^2} \mathrm{d}^2 q \exp(-\mathrm{i}\vec{q}\cdot(\vec{s} - \Delta\vec{s}(z)))$$
$$\times \exp\left(-\frac{1}{4}\vec{q}^{\,T}\beta\vec{q}\right)\exp\left(\tau(z)W_0(z)\exp\left(-\frac{1}{4}\vec{q}^{\,T}\boldsymbol{\alpha}\vec{q}\right)\right), \tag{16}$$

where $\tau(z) = \int_0^z \rho_{\mathrm{n}}(z)\sigma_{\mathrm{ext}}(z)\,\mathrm{d}z$ is an optical distance, $\tau'(z) = \int_0^z (\rho_{\mathrm{n}}(z)\sigma_{\mathrm{ext}}(z) + \mu(z))\,\mathrm{d}z$ is the extinction length and $\Delta\vec{s}(z) = \int_0^z \vec{b}(z)\,\mathrm{d}z$ is the total beam deflection. Next, by using the Taylor expansion

$$\exp\left(\tau(z)W_0(z)\exp\left(-\frac{1}{4}\vec{q}^{\,T}\boldsymbol{\alpha}\vec{q}\right)\right) = \sum_{k=0}^{\infty}\left[\frac{1}{k!}\left(\tau(z)W_0(z)\exp\left(-\frac{\vec{q}^{\,T}\boldsymbol{\alpha}\vec{q}}{4}\right)\right)^k\right] \tag{17}$$

the following expression is obtained from equation (16):

$$I(z, \vec{\rho}, \vec{s}) = \frac{I_0}{(2\pi)^2}\exp(-\tau'(z))\iint_{\mathbb{R}^2} \mathrm{d}^2 q \exp(-\mathrm{i}\vec{q}\cdot(\vec{s} - \Delta\vec{s}(z)))$$
$$\cdot \sum_{k=0}^{\infty}\left[\frac{(\tau(z)W_0(z))^k}{k!}\exp\left(-\frac{\vec{q}^{\,T}[\beta + \boldsymbol{\alpha}k]\vec{q}}{4}\right)\right]. \tag{18}$$

Now let us define

$$\mathbf{C} \triangleq [\beta + \boldsymbol{\alpha}k] = \frac{1}{2}\mathrm{diag}\left(\frac{1}{\beta_x} + \frac{k}{\alpha_{\mathrm{p}}}, \frac{1}{\beta_y} + \frac{k}{\alpha_{\mathrm{p}}}\right). \tag{19}$$

Finally, we obtain the following solution for the intensity of the transmitted beam (after penetrating the object):

$$I(z, \vec{\rho}, \vec{s}) = I_0\exp(-\tau'(z))\sum_{k=0}^{\infty}\frac{(\tau(z)W_0(z))^k}{k!}\frac{1}{2\pi|\mathbf{C}|^{1/2}}$$
$$\times \exp\left(-\frac{1}{2}(\vec{s} - \Delta\vec{s}(z))^T\mathbf{C}^{-1}(\vec{s} - \Delta\vec{s}(z))\right). \tag{20}$$

It should be noted that this solution assumes an infinite medium; thus, it would not be strictly valid at the edges of the object. However, we anticipate that this issue will not have major significance in practical imaging applications.

It is interesting to note that the term in the summation in equation (20) is related to a Poisson probability law. Indeed, in the simpler case of an incident plane wave, the corresponding portion of this equation can roughly be derived by a statistical argument in which the random distribution of scatterers is modelled as a Poisson process (Dexter and Beeman 1949).

5. MIR parameters

In MIR, measurements of intensity are made at many angular positions s_x of the analyser crystal. These measurements can be described by

$$I_m(\vec{\rho}, s_x) = \int_{-\infty}^{\infty}\mathrm{d}s_x'\int_{-\infty}^{\infty}\mathrm{d}s_y'\, I(Z, \vec{\rho}, \vec{s}')R(s_x - s_x'), \tag{21}$$

where $R(s_x)$ is the rocking curve of the analyser crystal and Z is the thickness of the object at image location $\vec{\rho}$. We define the moments of the rocking curve as follows:

$$\int_{-\infty}^{\infty} R(s_x)\,\mathrm{d}s_x \triangleq R_T, \qquad \int_{-\infty}^{\infty} s_x R(s_x)\,\mathrm{d}s_x = 0, \qquad \int_{-\infty}^{\infty} s_x^2 R(s_x)\,\mathrm{d}s_x \triangleq w_R. \tag{22}$$

Our assumption that the rocking curve has zero centroid simply reflects choice of the coordinate system to align with this direction.

Now we derive the values of the three MIR parameters based on the predicted intensity function of the transmitted beam. In the following, we assume that the number of measurements is sufficiently large to avoid sampling artefacts. The impact of sampling on the accuracy of these parameters will be studied in a future paper.

5.1. Absorption image

It is easy to show that, after passing through the object, the total measured intensity of the beam at image location $\vec{\rho}$ is

$$\begin{aligned} I_T(\vec{\rho}) &= \int_{-\infty}^{\infty} I_m(\vec{\rho}, s_x)\,\mathrm{d}s_x \\ &= I_0 R_T \exp\left(-\int_0^Z (\rho_\mathrm{n}(z)\sigma_\mathrm{a} + \mu(z))\,\mathrm{d}z\right) \\ &= I_0 R_T \exp\left(-\int_0^Z \bar{\mu}(z)\,\mathrm{d}z\right), \end{aligned} \tag{23}$$

where $\bar{\mu}(z) \triangleq \rho_\mathrm{n}(z)\sigma_\mathrm{a} + \mu(z)$ is the net linear absorption of the medium (including the embedded scatterers). Equation (23) is simply an expression of Beer's law, which can be inverted in the usual way to obtain

$$A_\mathrm{MIR}(\vec{\rho}) \triangleq -\ln\left(\frac{I_T(\vec{\rho})}{I_0 R_T}\right) = \int_0^z \bar{\mu}(z)\,\mathrm{d}z. \tag{24}$$

Thus, as expected for this case, the MIR absorption image A_MIR is a line integral of the net linear absorption coefficient of the object.

5.2. Refraction-angle image

In MIR, the net refraction angle of the beam by the object, denoted by Δs_MIR, is inferred at every pixel by estimating the angular shift of the centroid of the beam's angular intensity spectrum. We have defined the coordinate system such that, with the object absent, the centroid is at $s_x = 0$; therefore, the shift is simply the value of the centroid of the measured intensity when the object is placed in the beam. Therefore, using equations (20) and (21), one can readily show that the measured refraction-angle image is

$$\Delta s_\mathrm{MIR}(\vec{\rho}) \triangleq \frac{1}{I_T}\int_{-\infty}^{\infty} s_x I_m(\vec{\rho}, s_x)\,\mathrm{d}s_x = \int_0^z b_x(z)\,\mathrm{d}z, \tag{25}$$

where $b_x(z)$ is defined as in equation (4). Thus, the MIR refraction image is seen to be the line integral of the scaled refractive-index gradient $b_x(z)$.

5.3. USAXS-parameter image

In MIR, we use the second central moment of the beam's angular intensity spectrum to measure beam divergence induced by the presence of scatterers. To determine the effect of

the object alone, we must subtract the second central moment of the intrinsic rocking curve of the imaging optics $W_T = (1/\beta_x) + w_R$ (i.e. the overall reflectivity function with the object absent), as explained in Wernick *et al* (2005). Thus, the MIR USAXS-parameter image is defined as

$$w_{\mathrm{MIR}}(\vec{\rho}) \triangleq \frac{1}{I_T}\int_{-\infty}^{\infty}\left(s_x - \int_0^z b_x(z)\,\mathrm{d}z\right)^2 I_m(\vec{\rho}, s_x)\,\mathrm{d}s_x - W_T. \tag{26}$$

Substituting from equation (21) into (26), one can show that, like the absorption and refraction parameters, the MIR USAXS parameter w_{MIR} is also a line integral; specifically, it is given by

$$w_{\mathrm{MIR}}(\vec{\rho}) = \int_0^Z \left[\frac{\rho_{\mathrm{n}}(z)\sigma_{\mathrm{s}}(z)}{2\alpha_{\mathrm{p}}}\right]\mathrm{d}z. \tag{27}$$

A detailed derivation of equation (27) is lengthy, so we defer this calculation to appendix B.

5.4. Summary of results

Equations (24), (25) and (27) show that (1) each of the MIR image parameters is the line integral of some property of the object, and (2) the three MIR images separately and independently depict the effects of absorption, refraction and USAXS. We have assumed this separability property to be true in our previous work, but it has not before been demonstrated through an analysis of beam propagation. Equation (27) provides an explanation of the scattering property measured by the USAXS image. When imaging biological tissue, which is not truly a collection of discrete scatterers, equation (27) can be interpreted as a particle-equivalent tissue model, which may be helpful for interpreting the USAXS parameter in relation to the object's microstructure.

6. Experimental validation

In this section, we will validate our theoretical model experimentally and through computer simulations.

6.1. Imaging experiment

First, we performed a simple experiment using the phantom shown in figure 5. This experiment was described briefly in a previous paper of ours (Brankov *et al* 2004), where we empirically demonstrated the linearity of the MIR USAXS parameter, but without any theoretical explanation. Our purpose here is to verify that the theoretical model presented in this paper is consistent with these previous experimental results.

In the experiment, a wedge-shaped Lucite container was filled with a suspension of $m_{\mathrm{PMMA}} = 1.61$ g of polymethylmethacrylate (PMMA) microspheres (scatterers) in $m_{\mathrm{G}} = 10.01$ g of glycerin. The mean radius R of the microspheres was 3.25 μm with the standard deviation of 3.25 μm. The densities of PMMA and glycerin are $\rho_{\mathrm{PMMA}} = 1.19\ \mathrm{g\ cm^{-3}}$ and $\rho_{\mathrm{G}} = 1.26\ \mathrm{cm^{-3}}$, respectively; thus, the volume density of the scatterers was calculated as $\rho_{\mathrm{n}} = V\big/\left(\frac{4}{3}R^3\pi\right) = 1.01 \times 10^9\ \mathrm{cm^{-3}}$, where V is the total volume of the mixture given by $V = \rho_{\mathrm{G}}m_{\mathrm{G}} + \rho_{\mathrm{PMMA}}m_{\mathrm{PMMA}} = 14.52\ \mathrm{cm^{-3}}$. The difference between the refractive indices of PMMA and glycerin is $\delta = 5.4 \times 10^{-8}$. For spherical scatterers, it can be shown (von Nardroff 1926) that angular beam broadening due to a single scatterer is described by $\alpha_{\mathrm{p}} = \left[4\delta^2 \ln\left(\frac{2}{\delta} + 1\right)\right]^{-1} = 4.91 \times 10^{12}$. Here it is worth noting that μ is calculated as $\mu = \left(\frac{\mu_{\mathrm{G}}}{\rho_{\mathrm{G}}}\right)\frac{m_{\mathrm{G}}}{V}$, where $\mu_{\mathrm{G}}/\rho_{\mathrm{G}}$ is the mass absorption coefficient of glycerin and that $\sigma_{\mathrm{a}} = \left(\frac{\mu_{\mathrm{PMMA}}}{\rho_{\mathrm{PMMA}}}\right)\frac{m_{\mathrm{PMMA}}}{\rho_{\mathrm{n}}V}$, where $\mu_{\mathrm{PMMA}}/\rho_{\mathrm{PMMA}}$ is the mass absorption coefficient of PMMA.

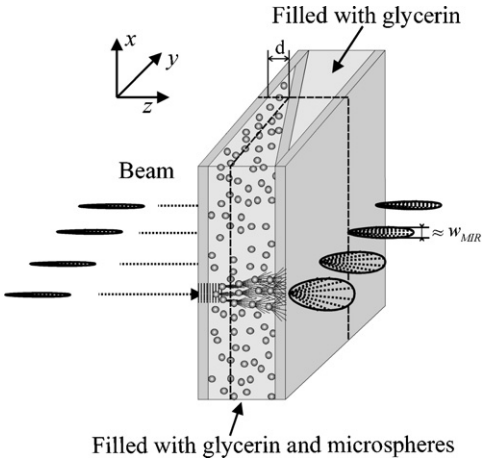

Figure 5. Experimental phantom for validation of theoretical model.

The phantom was imaged by the MIR method at 18 keV using the X-15A beamline of the National Synchrotron Light Source at Brookhaven National Laboratory, and a USAXS parameter image was computed from the data using the MIR method.

For comparison, we predicted the USAXS parameter image using the theory developed in this paper (equation (27)). Based on specifications of the microspheres provided by the manufacturer, we assumed the particle distribution to be a truncated normal distribution, denoted by $P(R)$, with the range 0.1–6.4 μm and standard deviation of 3.25 μm. One can compute the average beam divergence according to

$$\overline{w_{\mathrm{MIR}}(\vec{\rho})} = \frac{Z}{\alpha_{\mathrm{p}}} \int_{0.1\,\mu\mathrm{m}}^{6.4\,\mu\mathrm{m}} P(R)\rho_{\mathrm{n}}(R)\sigma_{\mathrm{s}}(R)\,\mathrm{d}R, \tag{28}$$

where it can be shown easily that

$$\rho_{\mathrm{n}}(R) = \frac{3}{4\pi R^3}\left(\frac{m_{\mathrm{G}}}{m_{\mathrm{PMMA}}}\frac{\rho_{\mathrm{PMMA}}}{\rho_{\mathrm{G}}} + 1\right)^{-1} \tag{29}$$

and, by definition, $\sigma_{\mathrm{s}}(R) = R^2\pi$.

Figure 6 shows good agreement between the experimental results and theoretical prediction of the USAXS parameter as a function of object thickness. Furthermore, a least-squares test of linearity of the USAXS parameter shows the relationship to be significant at the level $p < 10^{-4}$.

6.2. Computer simulation

To further validate our theoretical calculations, we developed a computer simulation which makes the same physical assumptions as the theory, except that spherical scatterers are used (which do not have a Gaussian phase function). Specifically, we modelled a phantom similar to the one used in the experiment described above, but we now assume a uniform particle size. Figure 7 shows projected views through regions of this simulated wedge phantom at various thicknesses of the object. Where the wedge is thick ($Z = 100$ μm), many scatterers lie along the line of sight. In thin regions ($Z = 1$ μm), fewer scatters appear in the projected view. The images in figure 7 are refraction-angle values, with white signifying upward refraction, and black signifying downward refraction.

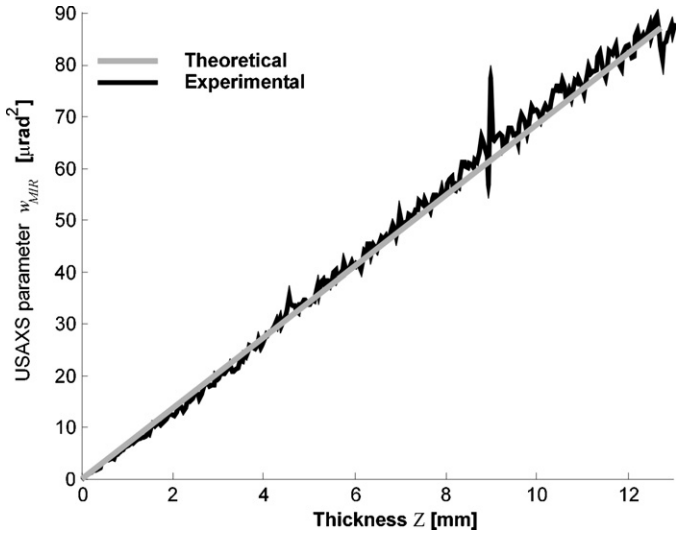

Figure 6. USAXS parameter versus object thickness: comparison of experimental results with theoretical prediction.

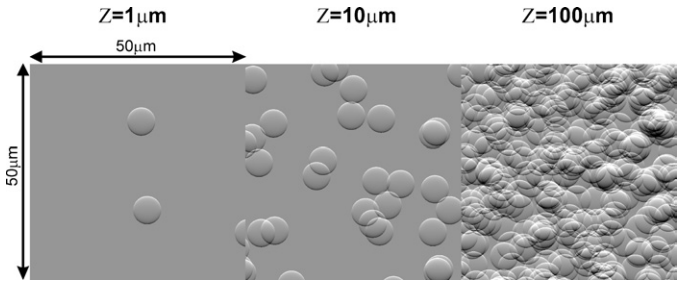

Figure 7. Projected views of the particle distribution through various thicknesses within the simulated wedge phantom. The region of interest is the size of one pixel; thus, the objects shown are not spatially resolved by the imaging method. Instead, the average net divergence of the beam is measured. Intensity values shown are proportional to the angle of refraction experienced by a ray traversing the corresponding position within the phantom. White indicates upward refraction, and black indicates downward refraction.

In the simulation, we used geometrical-optics ray tracing to predict the transmitted beam intensity. We then used equation (27) to predict the MIR USAXS parameter for this particle distribution. Figure 8 shows the USAXS parameter as a function of object thickness obtained by computer simulation and theoretical prediction. Again, there is good agreement; however, there is a slight discrepancy between the theoretical and simulated curves due to the non-Gaussian phase function of the scatterers and randomness in the specific statistical realization of the spatial distribution of the scatterers.

In each of these experiments (based on real imaging data and computer simulations), we also validated our theoretical models of the absorption parameter and refraction parameter. Since these parameters are comparatively simple and well understood, we have omitted the details of these validation studies. However, we have reviewed them briefly in Wernick *et al* (2005).

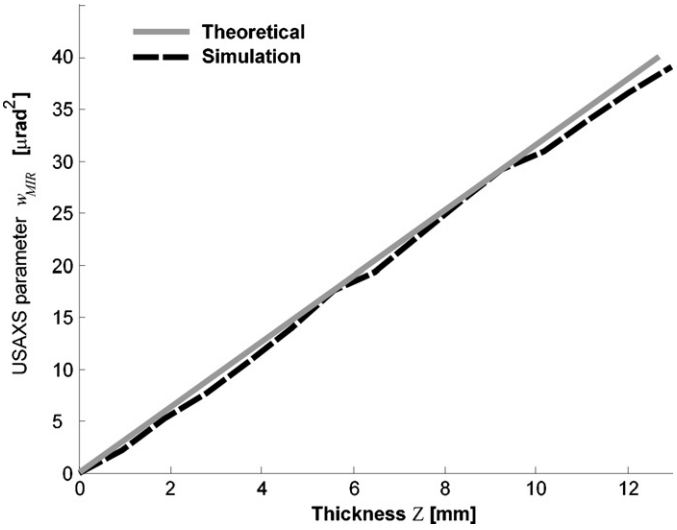

Figure 8. USAXS parameter versus object thickness: comparison of computer simulation with theoretical prediction.

7. Conclusion

While the MIR imaging method has shown promising results, it has not before had a solid theoretical underpinning. In this paper, using radiative transport theory, we explain the origin of the three MIR images, and derive expressions for the measured MIR parameters in terms of the fundamental properties of the object. Most importantly, we show that all three MIR parameters are linear in object thickness, an important requirement for computed tomography applications. Our analysis also demonstrates that MIR can truly separate the effects of absorption, refraction and USAXS into three respective images.

Acknowledgments

This research was supported by NIH/NIAMS grant AR48292 and NIH/NCI grant CA111976. Use of the X15A beamline at the National Synchrotron Light Source, Brookhaven National Laboratory was supported by the US Department of Energy contract No. DE-AC02-98CH10886 and by the Brookhaven National Laboratory LDRD 05-057. We thank Carol Muehleman and Jun Li for leading the joint imaging study that produced the images shown in figure 2.

Appendix A. Derivation of the refraction term in transport equation (3)

Here we derive the refraction term in transport equation (3). In a stratified medium the refractive index is given by (see figure A1)

$$n(x', y', z') = n_0 + \begin{bmatrix} n_x f(z') & 0 & 0 \\ 0 & n_y f(z') & 0 \\ 0 & 0 & 0 \end{bmatrix} \begin{bmatrix} x' \\ y' \\ z' \end{bmatrix}. \tag{30}$$

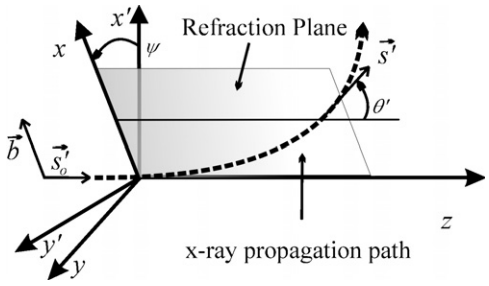

Figure A1. Illustration of rotation of an arbitrary coordinate system (x, y, z) into the refraction plane, which coincides with the (x', z)-plane of a new coordinate system.

The optical Lagrangian in the (x', y', z') coordinate system (figure A1) is as follows:

$$L(x', y', z') = n(x', y', z')(1 + \dot{x}'^2 + \dot{y}'^2)^{1/2}, \tag{31}$$

where

$$\dot{x} = \frac{\mathrm{d}x}{\mathrm{d}z} = \tan\theta_x, \qquad \dot{y} = \frac{\mathrm{d}y}{\mathrm{d}z} = \tan\theta_y \tag{32}$$

are tangents of deflection angles of the beam in the x and y directions. Applying Fermat's principle to the Lagrangian (31) we obtain the following differential equations for the beam deflection (Born and Wolf 1999):

$$\ddot{x}' = (1 + \dot{x}'^2 + \dot{y}'^2)\left(\frac{\partial \ln n}{\partial x'} - \dot{x}'\frac{\partial \ln n}{\partial z'}\right) \tag{33}$$

$$\ddot{y}' = (1 + \dot{x}'^2 + \dot{y}'^2)\left(\frac{\partial \ln n}{\partial y'} - \dot{y}'\frac{\partial \ln n}{\partial z'}\right). \tag{34}$$

Dividing (33) by (34) and using simple separation of variables one can show that the angle ψ between the $x'z'$-plane and the refraction plane is constant, i.e.,

$$\psi = \tan^{-1}\left(\frac{\mathrm{d}y}{\mathrm{d}x}\right) = \tan^{-1}\left(\frac{n_y}{n_x}\right) = \text{const.} \tag{35}$$

Thus, without loss of generality, one can rotate the coordinate system to coincide with the refraction plane, as shown in figure A1. As a result of this rotation, the $x'z'$-plane becomes the refraction plane xz and the x-axis becomes parallel to the refractive-index gradient ($\vec{b}$) direction.

As a result of this rotation, equations (33) and (34) can be rewritten as a single equation in terms of x and y:

$$\ddot{x} = (1 + \dot{x}^2)\left(\frac{\partial \ln n}{\partial x} - \dot{x}\frac{\partial \ln n}{\partial z}\right). \tag{36}$$

In the small-angle approximation, $\dot{x}^2 \approx \theta^2 \ll 1$, and equation (36) becomes

$$\ddot{x} = \frac{\partial \ln n}{\partial x} - \dot{x}\frac{\partial \ln n}{\partial z}, \tag{37}$$

which can be simplified further using small angle approximation and equation (32) to obtain

$$\ddot{x} = \frac{\partial \ln n}{\partial x}\left(1 - \dot{x}\frac{\partial \ln n/\partial z}{\partial \ln n/\partial x}\right) = \frac{\partial \ln n}{\partial x}(1 - \dot{x}^2) \approx \frac{\partial \ln n}{\partial x}. \tag{38}$$

Finally, equation (38) can be integrated once over z to obtain

$$\mathrm{d}\dot{x} = \frac{\partial \ln n}{\partial x}\mathrm{d}z. \tag{39}$$

Since, the refraction process takes place within a fixed plane, equation (39) can be rewritten in vector form as follows:

$$\mathrm{d}\vec{s} = (\nabla_{\vec{r}'} \ln n(\vec{r}))\,\mathrm{d}z. \tag{40}$$

Therefore, the $\partial/\partial z$ operator takes the following form:

$$\frac{\partial}{\partial z} = \nabla_{\vec{r}'} \ln n(\vec{r}) \cdot \frac{\mathrm{d}}{\mathrm{d}\vec{s}} = \nabla_{\vec{r}} \ln n(\vec{r}) \cdot \nabla_{\vec{s}}. \tag{41}$$

When applied to the specific intensity, this operator will produce the refraction term (fourth term) of transport equation (3):

$$\frac{\partial I(z, \vec{\rho}, \hat{\vec{s}})}{\partial z} = \nabla_{\vec{r}} \ln n(\vec{r}) \cdot \nabla_{\hat{\vec{s}}} I(z, \vec{\rho}, \hat{\vec{s}}) = \vec{b} \cdot \nabla_{\hat{\vec{s}}} I(z, \vec{\rho}, \hat{\vec{s}}). \tag{42}$$

Appendix B. Derivation of the MIR UXAXS parameter $w_{\mathrm{MIR}}(\vec{\rho})$ (equation (27))

We begin by writing equation (21) in the following form:

$$I_m(\vec{\rho}, s_x) = \int_{-\infty}^{\infty} \mathrm{d}s'_x \int_{-\infty}^{\infty} \mathrm{d}s'_y\, I(Z, \vec{\rho}, \vec{s}') R(s_x - s'_x), \tag{43}$$

which can be expanded using equation (20) and integrated with respect to $\mathrm{d}s'_y$ yielding

$$I_m(z, \vec{\rho}, s_x) = I_0 \exp(-\tau'(z)) \sum_{k=0}^{\infty} \frac{(\tau(z) W_0(z))^k}{k!} \frac{1}{\sqrt{2\pi\left[\frac{1}{2}\left(\frac{1}{\beta_x} + \frac{k}{\alpha_p}\right)\right]}}$$
$$\times \int_{-\infty}^{\infty} \mathrm{d}\vec{s}'_x \exp\left[-\frac{(s'_x - \Delta s_x(z))^2}{2\left[\frac{1}{2}\left(\frac{1}{\beta_x} + \frac{k}{\alpha_p}\right)\right]}\right] R(s_x - s'_x). \tag{44}$$

Note that the integral is a convolution of a Gaussian function with $R(s_x)$. Now let us define

$$\mathrm{N}\left(s_x, \Delta s_x(z), \frac{1}{2}\left(\frac{1}{\beta_x} + \frac{k}{\alpha_\mathrm{p}}\right)\right) \triangleq \frac{1}{\sqrt{2\pi\left[\frac{1}{2}\left(\frac{1}{\beta_x} + \frac{k}{\alpha_\mathrm{p}}\right)\right]}} \exp\left(-\frac{(s_x - \Delta s_x(z))^2}{2\left[\frac{1}{2}\left(\frac{1}{\beta_x} + \frac{k}{\alpha_\mathrm{p}}\right)\right]}\right), \tag{45}$$

which allows us to rewrite equation (44) in the following form:

$$I_m(z, \vec{\rho}, s_x) = I_0 \exp(-\tau'(z)) \sum_{k=0}^{\infty} \frac{(\tau(z) W_0(z))^k}{k!} \mathrm{N}\left(s_x, \Delta s_x(z), \frac{1}{2}\left(\frac{1}{\beta_x} + \frac{k}{\alpha_\mathrm{p}}\right)\right) * R(s_x), \tag{46}$$

where $*$ denotes a convolution operator. Now from equations (26) and (46) we have

$$w_{\mathrm{MIR}}(z, \vec{\rho}) = \exp(-\tau(z) W_0(z)) \sum_{k=0}^{\infty} \frac{(\tau(z) W_0(z))^k}{k!}$$
$$\cdot \int_{-\infty}^{\infty} (s_x - \Delta s_x(z))^2 \mathrm{N}\left(s_x, \Delta s_x(z), \frac{1}{2}\left(\frac{1}{\beta_x} + \frac{k}{\alpha_\mathrm{p}}\right)\right) * R(\vec{s}_x)\,\mathrm{d}\vec{s}_x - W_T, \tag{47}$$

where $W_T = (1/\beta_x) + w_R$. Performing the integration with respect to s_x yields

$$w_{\mathrm{MIR}}(z, \vec{\rho}) = \exp(-\tau(z)W_0(z)) \left[\sum_{k=0}^{\infty} \frac{(\tau(z)W_0(z))^k}{k!} \frac{1}{2} \left(\frac{1}{\beta_x} + \frac{k}{\alpha_{\mathrm{p}}} \right) + w_R \right] - W_T. \tag{48}$$

Now since

$$\sum_{k=0}^{\infty} \frac{(\tau(z)W_0(z))^k}{k!} = \exp(\tau(z)W_0(z)) \tag{49}$$

and

$$\sum_{k=0}^{\infty} \frac{(\tau(z)W_0(z))^k}{k!} k = \tau(z)W_0(z)\exp(\tau(z)W_0(z)_0) \tag{50}$$

we obtain

$$w_{\mathrm{MIR}}(Z, \vec{\rho}) = \frac{1}{2\alpha_{\mathrm{p}}} \int_0^z \rho_{\mathrm{n}}(z)\sigma_{\mathrm{s}}(z)\,\mathrm{d}z, \tag{51}$$

which is the key result presented in equation (27).

References

Born M and Wolf E 1999 *Principles of Optics* 7th edn (Oxford: Pergamon)

Brankov J G, Wernick M N, Chapman D, Zhong Z, Muehleman C, Li J and Anastasio M A 2004 Multiple-image computed tomography *Proc. IEEE Int. Symp. Biomed. Imaging* pp 948–51

Chapman D, Thomlinson W, Johnston R E, Washburn D, Pisano E, Gmür N, Zhong Z, Menk R, Arfelli F and Sayers D 1997 Diffraction enhanced x-ray imaging *Phys. Med. Biol.* **42** 2015–25

Dexter D L and Beeman W W 1949 Multiple diffuse small angle scattering of X-rays *Phys. Rev.* **76** 1782–6

Ishimaru A 1997 *Wave Propagation and Scattering in Random Media* (New York: IEEE)

Pagot E, Cloetens P, Fiedler S, Bravin A, Coan P, Baruchel J, Hartwig J and Thomlinson W 2003 A method to extract quantitative information in analyzer-based x-ray phase contrast imaging *Appl. Phys. Lett.* **82** 3421–3

Rigon L, Besch H-J, Arfelli F, Menk R-H, Heitner G and Besch H P 2003 A new DEI algorithm capable of investigating sub-pixel structures *J. Phys. D: Appl. Phys.* **36** 107–12

Schmitt J M and Kumar G 1998 Optical scattering properties of soft tissue: a discrete particle model *Appl. Opt.* **37** 2788–97

von Nardroff R 1926 Refraction of x-rays by small particles *Phys. Rev.* **28** 240–6

Wernick M N, Wirjadi O, Chapman D, Oltulu O, Zhong Z and Yang Y 2002 Preliminary investigation of a multiple-image radiography method *Proc. IEEE Int. Symp. Biomed. Imaging* 129–32

Wernick M N, Wirjadi O, Chapman D, Zhong O Z, Galatsanos N, Yang Y, Brankov J G, Oltulu O, Anastasio M A and Muehleman C 2003 Multiple-image radiography *Phys. Med. Biol.* **48** 3875–95

Wernick M N, Brankov J G, Chapman D, Yang Y, Pisano E, Parham C, Muehleman C, Zhong Z and Anastasio M A 2005 Multiple-image radiography and computed tomography *Proc. SPIE* **5535** 369–79